

Manuscript version: Author's Accepted Manuscript

The version presented in WRAP is the author's accepted manuscript and may differ from the published version or Version of Record.

Persistent WRAP URL:

<http://wrap.warwick.ac.uk/131249>

How to cite:

Please refer to published version for the most recent bibliographic citation information. If a published version is known of, the repository item page linked to above, will contain details on accessing it.

Copyright and reuse:

The Warwick Research Archive Portal (WRAP) makes this work by researchers of the University of Warwick available open access under the following conditions.

Copyright © and all moral rights to the version of the paper presented here belong to the individual author(s) and/or other copyright owners. To the extent reasonable and practicable the material made available in WRAP has been checked for eligibility before being made available.

Copies of full items can be used for personal research or study, educational, or not-for-profit purposes without prior permission or charge. Provided that the authors, title and full bibliographic details are credited, a hyperlink and/or URL is given for the original metadata page and the content is not changed in any way.

Publisher's statement:

Please refer to the repository item page, publisher's statement section, for further information.

For more information, please contact the WRAP Team at: wrap@warwick.ac.uk.

Feasibility Studies of a Converter-free Grid-connected Offshore Hydrostatic Wind Turbine

Shuyue Lin, Xiaowei Zhao and Xin Tong

Abstract—Owing to the increasing penetration of renewable power generation, the modern power system faces great challenges in frequency regulations and reduced system inertia. Hence, renewable energy is expected to take over part of the frequency regulation responsibilities from the gas or hydro plants and contribute to the system inertia. In this paper, we investigate the feasibility of frequency regulation by the offshore hydrostatic wind turbine (HWT). The simulation model is transformed from NREL (National Renewable Energy Laboratory) 5-MW gearbox-equipped wind turbine model within FAST (fatigue, aerodynamics, structures, and turbulence) code. With proposed coordinated control scheme and the hydrostatic transmission configuration of the HWT, the ‘continuously variable gearbox ratio’ in turbulent wind conditions can be realised to maintain the constant generator speed, so that the HWT can be connected to the grid without power converters in-between. To test the performances of the control scheme, the HWT is connected to a 5-bus grid model and operates with different frequency events. The simulation results indicate that the proposed control scheme is a promising solution for offshore HWT to participated in frequency response in the modern power system.

Index Terms—Hydrostatic wind turbine (HWT), frequency regulation, continuously variable transmission, \mathcal{H}_∞ loop-shaping.

I. INTRODUCTION

Due to the efforts towards a low-carbon world, the recent years witness a rapid development in renewable energy, in particularly wind energy. By the end of 2018, the cumulative installed wind energy capacity had reached 597 GW. It is anticipated to have new installations of at least 55 GW (onshore and offshore) each year until 2023 [1], [2]. In some EU countries such as Denmark, Portugal, Ireland and Germany, the wind power penetration rate reached over 20% in 2018, amongst which Denmark’s wind energy shares the highest proportion (41%) in its electricity demand [3]. The wind turbines currently do not directly contribute to system inertia because their power converters prevent the generators from responding to system frequency changes [4]. However, the frequency variation rate during the imbalance between power supply and load demands is highly related to the system inertia which therefore reduces as the growth of wind power penetration rate. This has brought great challenges and aroused wide concerns on the system stability.

In power generation industry, the frequency regulation technique usually includes inertia support [5], [6], primary frequency control [7], and the secondary automatic generation control (AGC) [8]. It is usually implemented by gas or hydro

plant where traditional synchronous generators are applied. In wind power generation industry, the doubly fed induction generators (DFIGs) with gearbox are widely applied in land-base wind turbine systems, while multi-pole synchronous generators without (or sometimes with) gearbox are usually selected in offshore cases. However, the power converters are required in both configurations for the wind turbine - grid connection, so that no direct inertia support can be provided by these turbines. Some researches proposed the concept of emulated inertia response, which is to release the kinematic energy stored in generator rotor for the grid when system frequency drops [9], [10]. However, compared to the direct inertia response by the gas or hydro plant, the emulated inertia support increases the complexity of the power converter control system thus may lead to the reduction in system reliability. Moreover, some literature investigated the auxiliary control schemes for the wind turbines to provide system frequency response, such as droop control to provide emulated primary frequency response [4] and de-rating control to reserves abundant power to manage the frequency variations [7], [11], [12]. It is usually achieved by redesigning the power control loop in rotor-side converter and deviating the blade pitch angles from the optimal position to ‘de-rate’ the power extraction [8], [13]. However, the accuracy of the regulation is influenced by the pitch response time, the turbulent wind and the amount of reserved wind power, thus resulting in low efficiency and reliability [14]. Besides, the de-rating operation violates the maximum power point tracking (MPPT) rules, which leads to the concern of energy waste and the economically trade-offs between the revenues from energy and regulation markets.

Hydrostatic wind turbine (HWT) may offer a better solution. The concept of HWT was proposed about 30 years ago, but it was not feasible at that time due to low power transmission efficiency [15]. With the development in hydrostatic transmission (HST) techniques, the efficiency has been largely improved. For the HST units based on the digital-displacement technique, the efficiency reached approximately 90% [16], which made the HWT feasible in industry [16]–[20]. In HWT, the gearbox drivetrain between the wind turbine rotor shaft and generator rotor shaft of a conventional wind turbine is replaced by the hydrostatic transmission (HST). HST introduces a new design dimension which potentially offers a more reliable transmission system for wind turbines [18], [21], aiming to provide continuously variable transmission ratio and reduce the maintenance costs by removing the troublesome gearbox and power converters with reduced wind turbine nacelle weight. In offshore case, the wind turbine is difficult to be maintained due to the weather and wave conditions. It would therefore benefit from the use of HST due to its reliability [20].

S. Lin, X. Zhao (Corresponding Author) and X. Tong are with the School of Engineering, University of Warwick, Coventry, CV4 7AL, United Kingdom, e-mail: shuyue.lin@warwick.ac.uk, xiaowei.zhao@warwick.ac.uk, xintong-carol@hotmail.com. This work was partially funded by the UK Engineering and Physical Sciences Research Council (grant number: EP/S000747/1).

HST offers a significant reduction in operation & maintenance cost of up to 56% in comparison with traditional gearbox drivetrain [20].

Current research on HWTs pays considerable attention to improve the power capture performances by applying advanced control strategies [22]–[24]. Only very few research is relevant to frequency control by HWT. In [25], a simple linear control scheme was applied for the proposed HST configurations which may maintain the generator speed. In [26], a control strategy was proposed to stabilise the generator speed for a HWT system with a specific configuration of multi-turbines sharing a common hydrostatic transmission drivetrain. However, both papers still only focused on the HWT itself without connecting HWT to the grid network. Therefore, the performance of the proposed control strategies could not be analysed in a network environment for grid frequency events study.

The present paper aims to investigate the feasibility of converter-free grid connection of an offshore HWT with frequency response ability through the proposed coordinated control scheme which includes the control of power transmission, energy storage and power generation with wind speed preview. In this way, the offshore HWT is expected to not only provide inertia response with its inherent inertia during frequency events, but also respond to frequency events properly even under strong turbulent wind. The proposed HWT structure is composed of a closed-loop oil circuit (connecting a pump and a motor), and an open-loop sea water circuit (connecting a pump-motor, a hydraulic accumulator, and a relief valve), see Fig. 1. The energy storage device (hydraulic accumulator) can be easily coupled to the HST of wind turbine and the HWT is connected to the grid via synchronous generator without power converters. We integrate the HWT model into a 5-bus network model and run the simulations under abnormal network event (trip one generator) with constant wind, and sudden load variations with strong turbulent wind. The simulation results indicate that the proposed control scheme is a promising solution for offshore HWT to participate in the frequency response with contribution to system inertia in modern electrical grid.

The paper is structured as follows: in Section II, we introduce system modelling. In Section III, we expatiate the coordinated control scheme. In Section IV, we conduct the simulations. Finally Section V concludes this paper.

II. SYSTEM MODELLING

The monopile hydrostatic wind turbine simulation model is transformed from the NREL (National Renewable Energy Laboratory) 5 MW gearbox-equipped monopile wind turbine model within FAST (fatigue, aerodynamics, structures, and turbulence) code [27]–[29]. The transformation procedure was detailed in [22]. The mathematical models of the hydrostatic transmission system will be introduced in this section. See Fig. 2 for the block diagram of the system modelling.

Variable displacement pump: The wind turbine rotor transforms the wind energy into the rotary motion then the variable displacement pump converts the mechanical power of rotor shaft to the hydraulic power in the high pressure oil line

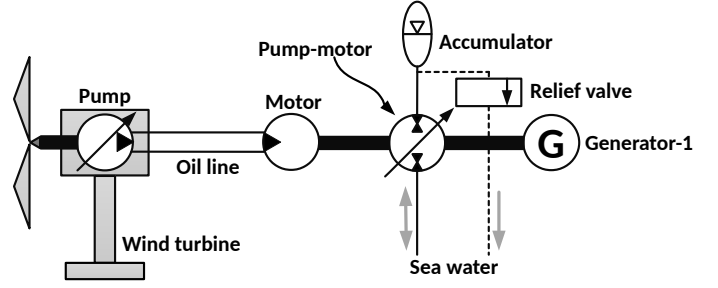


Fig. 1. Structure diagram of a hydrostatic wind turbine.

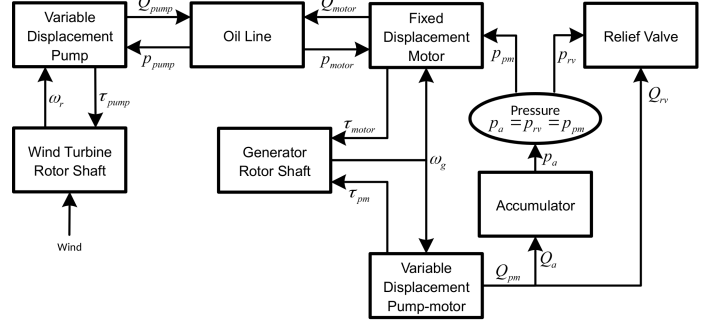


Fig. 2. Block diagram of a hydrostatic wind turbine.

[30]. The model of the pump is defined by the net generated volumetric flow rate Q_{pump} and the transmitted torque τ_{pump} :

$$Q_{pump} = D_p \omega_r - C_{sp} p_{pump}, \quad (1)$$

$$\tau_{pump} = (1 + C_{fp}) D_p p_{pump} + B_p \omega_r, \quad (2)$$

where D_p , ω_r , C_{sp} , p_{pump} , C_{fp} and B_p represent the pump volumetric displacement, wind turbine rotor speed, laminar leakage coefficient, the pressure difference across the pump, the Coulomb friction coefficient and the viscous damping coefficient of pump respectively.

The dynamics of the pump actuator is modelled as

$$\dot{D}_p = \frac{1}{T_p} \cdot (D_p^* - D_p), \quad (3)$$

where D_p^* represents the command of the pump volumetric displacement and T_p represents the time constant.

Wind turbine rotor shaft dynamics: The rotational dynamics of the wind turbine rotor shaft is modelled as:

$$\dot{\omega}_r = \frac{1}{J_r + J_p} \cdot [\tau_{aero}(\omega_r, \beta, v_{wind}) - \tau_{pump}], \quad (4)$$

where J_r and J_p are the rotational inertias of the wind turbine rotor and pump respectively, and τ_{aero} is the aerodynamic torque which depends on the rotor speed ω_r , blade pitch angle β and the rotor effective wind speed v_{wind} .

Fixed displacement motor: Fixed displacement motor transforms the hydraulic power from the high pressure oil line to the kinematic energy of the generator rotor shaft, whose model is similar to the pump with the only difference being the energy conversion direction. The net volumetric flow rate

Q_{motor} and transmitted torque of the motor τ_{motor} are

$$Q_{motor} = D_m \omega_g + C_{sm} p_{motor}, \quad (5)$$

$$\tau_{motor} = (1 + C_{fm}) D_m p_{motor} - B_m \omega_g, \quad (6)$$

where D_m , ω_g , C_{sm} , p_{motor} , C_{fm} and B_m represent the motor volumetric displacement, generator rotor speed, the laminar leakage coefficient, the pressure difference across the motor, the Coulomb friction coefficient and the viscous damping coefficient of motor, respectively.

Oil line: The power transmission of the hydraulic pipeline is modelled by a linear state-space model with assumption of constant pressure in low pressure line [22], [30]. Similar to [22], the number of modes are selected to be 10, thence, the line's model frequency is in the frequency range of [0, 93.12] Hz. The inputs to the pipeline are the flow rates of pump and motor, and the outputs of the pipeline are the pressure across the pump and motor:

$$\dot{\mathbf{x}}_l = \mathbf{A}_l \mathbf{x}_l + [\mathbf{B}_{l1} \ \mathbf{B}_{l2}] \begin{bmatrix} Q_{pump} \\ Q_{motor} \end{bmatrix}, \quad \begin{bmatrix} p_{pump} \\ p_{motor} \end{bmatrix} = \begin{bmatrix} \mathbf{C}_{l1} \\ \mathbf{C}_{l2} \end{bmatrix} \mathbf{x}_l \quad (7)$$

The matrices \mathbf{A}_l , \mathbf{B}_{l1} , \mathbf{B}_{l2} , \mathbf{C}_{l1} and \mathbf{C}_{l2} are defined in terms of the physical parameters of the hydraulic line, such as the pipe inner radius, fluid density, kinematic viscosity, etc. The modelling procedure has been detailed in [30], [31].

Variable displacement pump-motor: The fixed displacement motor and variable displacement pump-motor are both connected to the generator rotor shaft. The pump-motor keeps converting energy between kinematic and hydraulic energy, aiming to provides the desired power to the grid. The simplified model of pump-motor are expressed in the flow rate Q_{pm} and transmitted torque τ_{pm} [23]:

$$Q_{pm} = \eta_{Qpm} D_{pm} \omega_g, \quad \tau_{pm} = \eta_{\tau pm} D_{pm} p_{pm}, \quad (8)$$

where D_{pm} and p_{pm} represent the volumetric displacement of pump-motor and the pressure difference across the pump-motor, respectively. η_{Qpm} and $\eta_{\tau pm}$ represent the volumetric and mechanical efficiencies. Note that the sign of D_{pm} indicates the directions of the transmitted torque τ_{pm} and flow rate Q_{pm} , where positive sign implies the pump-motor is in pump motion. The dynamics of pump-motor actuator is modelled as

$$\dot{D}_{pm} = \frac{1}{T_{pm}} \cdot (D_{pm}^* - D_{pm}), \quad (9)$$

where D_{pm}^* is the command of the pump-motor displacement and T_{pm} is the time constant.

Generator rotor shaft dynamics: The rotary motion of the generator rotor shaft is modelled as:

$$\dot{\omega}_g = \frac{1}{J_m + J_{pm} + J_g} \cdot [\tau_m - (\tau_{pm} + \tau_g)]. \quad (10)$$

J_m , J_{pm} , J_g represents the rotational inertias of motor, pump-motor and generator, respectively. τ_g is the electrical torque of the generator.

Relief valve: The relief valve is installed to protect the accumulator from being overcharged. It is actually a controllable variable area hydraulic orifice, created by a cylindrical sharp-edged spool and a variable-area slot in a sleeve. The flow rate

Q_{rv} is defined as:

$$Q_{rv} = C_D A \sqrt{\frac{2}{\rho_{sw}}} \frac{p_{rv}}{\sqrt[4]{p_{rv}^2 + p_{cr}^2}}, \quad (11)$$

in which $p_{rv} = p_{pm} \cdot C_D$, and ρ_{sw} represent the flow discharge coefficient and the density of the seawater. p_{cr} is the minimum pressure for turbulent flow, when the block transitions from laminar to turbulent regime with $p_{cr} = \frac{\rho_{sw}}{2} \cdot \left(\frac{Re_{cr} \nu}{C_D \cdot 2 R_{ori}} \right)^2$. Re_{cr} , ν and R_{ori} are critical Reynolds number, seawater kinematic viscosity and the radius of the orifice, respectively.

Hydraulic accumulator: The accumulator here is a fixed volume cylindrical container, with a piston segregating the sea water from the inside pressurised gas. To simplify the performance of the accumulator, the adiabatic index is chosen to be 1, indicating an isothermal process. Thence, we have

$$V_0 = V_{hyd} + V_{gas}, \quad p_a = \frac{p_0 V_0}{V_{gas}} = \frac{p_0 V_0}{V_0 - \int \Delta Q_a d\tau}, \quad (12)$$

where V_0 , V_{hyd} and V_{gas} are the total volume of the accumulator, the seawater volume and gas volume in the accumulator, respectively. p_0 is the pressure in the accumulator when $V_{hyd} = 0$ and p_a is the pressure across the accumulator. Note that $p_a = p_{pm}$ due to the physical connection between pump-motor and accumulator. The dynamics of the sea water volume in the accumulator is modelled as $\dot{V}_{hyd} = \Delta Q_a$, where

$$\Delta Q_a = Q_{pm} - Q_{rv}. \quad (13)$$

The accumulator's state-of-charge (SOC) is defined as $SOC = \frac{V_{hyd}}{V_0}$, and the energy stored in accumulator E_a is expressed as $E_a = \int_0^t P_{acc} d\tau = p_0 V_0 \ln \frac{V_0}{V_{gas}} = p_0 V_0 \ln \frac{1}{1-SOC}$, where P_{acc} is the power flow of the accumulator.

III. CONTROL DESIGN

The wind turbine operation is divided into 4 regions according to the wind speed. For conventional wind turbines, when the wind is below cut-in speed (region 1) or above the cut-out speed (region 4), the wind turbine doesn't work. When the wind is above the cut-in speed and below rated speed (region 2), the blade pitch keeps at fine position and the rotor-side-converter controller regulates the electrical torque of the generator (usually doubly fed induction generator (DFIG)) to maximize the power extraction. When the wind speed is above the rated speed and below cut-out speed (region 3), the pitch controller is activated to maintain rated wind turbine rotor speed, and operates together with torque controller to achieve rated power extraction. In [22], the torque control for HWT was achieved by regulating the motor displacement (playing similar functions like adjusting the electrical torque of the generator in a traditional wind turbine), which indirectly adjusts the pump torque through the oil line to extract desired wind power. Like [22], the boundary speeds for these four region divisions in the present paper are 4 m/s (cut-in speed), 11.4 m/s (rated speed) and 25 m/s (cut-out speed) respectively.

Fig. 3 shows the interaction between the HWT system and controllers. There are 7 controllers in this HWT system, namely, pump torque controller, accumulator state-of-charge controller, wind turbine pitch controller, pump-motor torque

controller, Relief valve controller, frequency (active power) controller, and excitation controller. The details of these controllers and the their interactions are expatiated in this section.

A. Wind turbine pitch control

In our scheme, we would like to extract as much wind power as possible, and store the excessive power in the accumulator. However, once the accumulator is full, the wind turbine is forced to operate at the sub-optimal point, ensuring the generation balances the load demand. It can be achieved by deviating the blade pitch angle from its original position to reduce the power extraction. That is, different from the conventional wind turbines, the pitch control of HWT should be activated in both region 2 and region 3, in order to regulate the power extraction based on the SOC of the accumulator in all operation regions.

The power captured by the wind turbine can be expressed as $P = 0.5\rho_{air}\pi R^2 v_{wind}^3 C_p(\lambda, \beta)$ where ρ_{air} is the air density, R is the wind turbine rotor radius, v_{wind} is the rotor effective wind speed and $C_p(\lambda, \beta)$ is the power coefficient which depends on the tip-speed ratio λ and pitch angle β . Based on the definition of optimal tip-speed ratio $\lambda^* = \frac{\omega_r^* R}{v_{wind}}$, the optimal wind turbine rotor speed ω_r^* is linearly dependant on the rotor effective wind speed v_{wind} under MPPT operation in region 2. In this paper, the Light and Detection Ranging (LIDAR) simulator is mounted to the turbine for remote wind measurement. LIDAR simulator emits the laser wave to the atmosphere, which is then scattered by aerosol particles and partially returned to the LIDAR [32]. With proper computations based on the returned radiations, the rotor effective wind speed can be estimated, based on which the desired optimal wind turbine rotor speed can be obtained. See (14) for the computation of optimal wind turbine rotor speed, which is a tabulated function incorporating 5 control regions and serves as the reference for pitch controller.

$$\omega_r^* = \begin{cases} 12.1, & v_{wp} \geq 11.4; \\ 11.68 + \frac{12.1 - 11.68}{11.4 - 10.2}(v_{wp} - 10.2), & v_{wp} \in [10.2, 11.4); \\ 8.96 + \frac{11.68 - 8.96}{10.2 - 7.8}(v_{wp} - 7.8), & v_{wp} \in [7.8, 10.2); \\ 6.87 + \frac{8.96 - 6.87}{7.8 - 4}(v_{wp} - 4), & v_{wp} \in [4, 7.8); \\ 0, & v_{wp} < 4, \end{cases} \quad (14)$$

where v_{wp} represents the previewed rotor effective wind by LIDAR. ω_r^* is expressed in revolutions per minute (rpm) and v_{wp} is in meters per second (m/s). The control region division is in correspondence with torque control region division of NREL 5 MW baseline wind turbine model in [29]. From the top to bottom in (14) are region 3, region 2.5, region 2, region 1.5 and region 1 respectively, where region 1.5 and region 2.5 are generated for smooth transition between region 1, 2, 3.

A gain-scheduled PI controller with antiwindup (AW) compensator from [22], [30] is applied for wind turbine rotor speed regulation. The parameter $K_{p_{pit}}$ and $K_{I_{pit}}$ are set as

$$K_{p_{pit}} = -\frac{1.6167}{1 + \frac{\beta}{6.302336}}, \text{ and } K_{I_{pit}} = -\frac{0.6929}{1 + \frac{\beta}{6.302336}},$$

with antiwindup back-calculation coefficient 0.5 [22]. β represents the blade pitch angles in degree.

B. Pump torque control

An \mathcal{H}_∞ loopshaping torque controller is designed to govern the pump torque through adjusting the pump volumetric displacement D_p . The wind turbine operation in realistic scenarios is a complex nonlinear system with many uncertainties and interactions with other dynamics, such as wave conditions, tower vibrations, etc. In addition, the system order is reduced for the controller design. All above points inevitably leads to modelling error. We choose \mathcal{H}_∞ controller as it is robust and can largely mitigate the impact caused by the modelling error and uncertainties. The system equations are (3), (4), (7) and (10), which can be linearised at the operating point $(\bar{\omega}_r, \bar{v}_{wind}, \bar{\beta})$:

$$\dot{\hat{\mathbf{x}}}_{\tau c} = \mathbf{A}_{\tau c} \hat{\mathbf{x}}_{\tau c} + \mathbf{B}_{\tau c} \hat{D}_p^* + \mathbf{B}_{\tau cd} \hat{\mathbf{d}}, \quad (15)$$

$$\hat{\tau}_{pump} = \mathbf{C}_{\tau c} \hat{\mathbf{x}}_{\tau c} + D_{\tau c} \hat{D}_p^*, \quad (16)$$

in which $\hat{\mathbf{x}}_{\tau c} = \mathbf{x}_{\tau c} - \bar{\mathbf{x}}_{\tau c} = [\hat{\omega}_r \ \hat{D}_p \ \hat{\mathbf{x}}_l \ \hat{\omega}_g]^T$, $\hat{D}_p^* = D_p^* - \bar{D}_p$, $\hat{\mathbf{d}} = \mathbf{d} - \bar{\mathbf{d}} = [\hat{v}_{wind} \ \hat{\tau}_g \ \hat{\tau}_{pm}]^T$, and $\hat{\tau}_{pump} = \tau_{pump} - \bar{\tau}_{pump}$. The operating points are selected to be $\bar{\omega}_r = 10.3$ rpm, $\bar{v}_{wind} = 9$ m/s and $\bar{\beta} = 0^\circ$.

In (15) and (16), the matrices $\mathbf{A}_{\tau c}$, $\mathbf{B}_{\tau c}$, $\mathbf{B}_{\tau cd}$, $\mathbf{C}_{\tau c}$ and $D_{\tau c}$ are derived as

$$\mathbf{A}_{\tau c} = \begin{bmatrix} \frac{\partial \tau_{aero}}{\partial \omega_r} - B_p & \frac{-(1+C_{fp})C_{l1}\bar{\mathbf{x}}_l}{J_r + J_p} & \mathbf{A}_{13} & 0 \\ 0 & -\frac{1}{T_p} & \mathbf{0} & 0 \\ B_{l1}\bar{D}_p & B_{l1}\bar{\omega}_r & \mathbf{A}_{33} & B_{l2}D_m \\ 0 & 0 & \mathbf{A}_{43} & \frac{-B_m}{J_m + J_{pm} + J_g} \end{bmatrix},$$

where $\mathbf{A}_{33} = \mathbf{A}_l - C_{sp}B_{l1}C_{l1} + C_{sm}B_{l2}C_{l2}$,

$$\mathbf{A}_{13} = \frac{-(1+C_{fp})C_{l1}\bar{D}_p}{J_r + J_p}, \quad \mathbf{A}_{43} = \frac{(1+C_{fm})D_m C_{l1}}{J_m + J_{pm} + J_g},$$

$$\mathbf{B}_{\tau c} = \begin{bmatrix} 0 & \frac{1}{T_p} & \mathbf{0} & 0 \end{bmatrix}^T;$$

$$\mathbf{B}_{\tau cd} = \begin{bmatrix} \frac{\partial \tau_{aero}}{\partial v_{wind}} & 0 & 0 \\ 0 & 0 & 0 \\ \mathbf{0} & \mathbf{0} & \mathbf{0} \\ 0 & -\frac{1}{J_m + J_{pm} + J_g} & -\frac{1}{J_m + J_{pm} + J_g} \end{bmatrix};$$

$$\mathbf{C}_{\tau c} = [B_p \quad (1+C_{fp})C_{l1}\bar{\mathbf{x}}_l \quad (1+C_{fp})C_{l1}\bar{D}_p \quad 0];$$

and $D_{\tau c} = [0]$, respectively.

The system from pump displacement command D_p^* to pump torque τ_{pump} are denoted as a 24-order plant G_m with its state-space realisation $(\mathbf{A}_{\tau c}, \mathbf{B}_{\tau c}, \mathbf{C}_{\tau c}, D_{\tau c})$. We safely discard the last 8 states whose Hankel singular values are small and reduce the plant order to 16. It can be achieved by matching

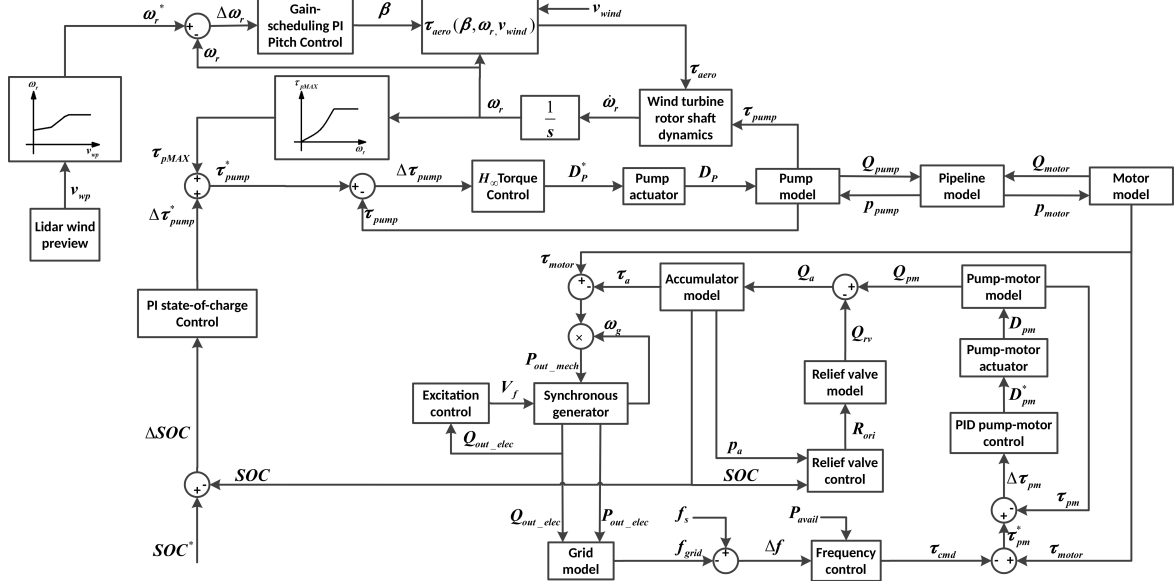


Fig. 3. Block diagram of interactions between controllers and the hydrostatic wind turbine system connecting to the grid.

DC-gain method using Matlab command *balred* [33], [34], which computes the reduced-order approximation of a LTI model while preserving the dynamics of the original system in the interested frequency range for control design purpose. By applying this method, the reduced-order system G_{mr} matches G_m very well at low frequency (< 73 Hz).

The \mathcal{H}_∞ controller K_τ is computed based on the reduced-order plant G_{mr} , aiming to match the singular value plot of the open loop transfer function $G_{mr}K_\tau$ with the desired loop shape G_d , with accuracy γ in the sense that

$$\underline{\sigma}(G_{mr}(j\omega)K_\tau(j\omega)) \leq \frac{1}{\gamma}\underline{\sigma}(G_d(j\omega)) \text{ for all } \omega > \omega_0, \text{ and,}$$

$$\underline{\sigma}(G_{mr}(j\omega)K_\tau(j\omega)) \leq \gamma\underline{\sigma}(G_d(j\omega)) \text{ for all } \omega > \omega_0,$$

where ω_0 is the crossover frequency of the singular value plot. The controller K_τ is designed by the Matlab function *loopsyn* [35], which computes the stabilising controller that best approximates the pre-specified desired open-loop shape. The desired open-loop shape G_d is selected to be

$$G_d = \frac{35000}{(s + 10^{-12})(s + 1000)}. \quad (17)$$

Fig. 4 represents the singular value plot of the open loop transfer function $G_{mr}K_\tau$ and its desired loop shape G_d . As we can see, with the control of K_τ , the open loop transfer function $G_{mr}K_\tau$ tracks the desired loop shape G_d very well. Fig. 5 shows the closed-loop step response which has no overshoot with a settling time of 0.1127 second.

C. Accumulator state-of-charge control

As mentioned in Section III-A, blade pitch angles will deviate from its original position once the accumulator is full. The pitch controller will maintain the wind turbine rotor speed ω_r according to (14), so the change in pump torque will result in the change in blade pitch angles. Hence, we regulate

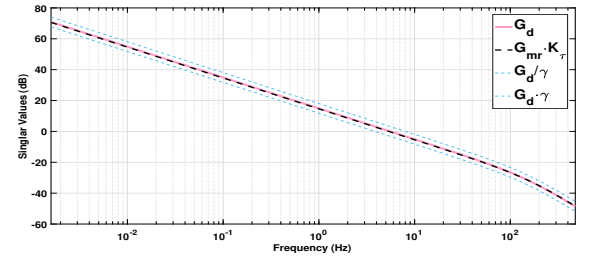


Fig. 4. Singular value plots of open loop transfer function $G_{mr}K_\tau$ and desired loop shape G_d .

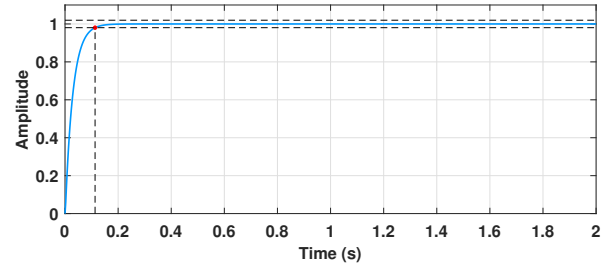


Fig. 5. Closed-loop step response of the \mathcal{H}_∞ loopshaping controller K_τ .

the pitch angle by redefining the pump torque reference according to accumulator's SOC, then the pitch angle will be automatically tuned to its desired position.

In this paper, the SOC of the accumulator is preserved at a relatively high level, to retain enough power in case of the higher load demand that the HWT cannot meet and also reduce the volume of the accumulator. The HWT extracts more power than grid request to charge the accumulator when wind is abundant, and reduce the power extraction if the accumulator is under overcharge risk. It means, the SOC of the accumulator serves as a feedback to adjust the power extraction, namely, adjusting the reference of pump torque τ_{pump}^* .

The NREL 5-MW conventional gearbox-equipped wind turbine provides the relationship between generator torque and turbine rotor speed under MPPT operation [29]. It can be modified and mapped from the generator-rotor-shaft side to the wind-turbine-rotor-shaft side, which reflects the relationship between pump torque under MPPT operation τ_{pMAX} and the wind turbine rotor speed ω_r :

$$\tau_{pMAX}(\omega_r) = \begin{cases} \frac{Pwr_0}{\omega_r} & \omega_r \geq 1.267; \\ K_0\omega_r^2 + \frac{Pwr_0}{1.267 - 1.255}(\omega_r - 1.255) & \omega_r \in [1.255, 1.267); \\ K_0\omega_r^2 & \omega_r \in [0.940, 1.255); \\ \frac{K_0\omega_r^2}{0.940 - 0.724} \cdot (\omega_r - 0.724) & \omega_r \in [0.724, 0.940); \\ 0 & \omega_r < 0.724, \end{cases} \quad (18)$$

Note that the region division is provided by [29], which is in accordance with (14). Pwr_0 represents the rated rotor power in Watt. Wind turbine rotor speed ω_r is radian per second (rad/s), τ_{pMAX} is in Newton meter (Nm) and K_0 is a constant. Then the available power Pwr_{avail} can be calculated as

$$Pwr_{avail} = \tau_{pMAX} \cdot \omega_r. \quad (19)$$

The accumulator's SOC indicates how much the pump torque should be deviated from τ_{pMAX} . It is marked as $\Delta\tau_{pump}^*$ in Fig. 3. We apply a PI controller to compute how much power extraction deviation ΔPwr from the available power Pwr_{avail} , and how much deviation ΔK from the constant K_0 . The difference $SOC^* - SOC$ is denoted as ΔSOC where SOC^* is a constant:

$$\Delta Pwr = K_{pSOC} \Delta SOC + K_{iSOC} \int \Delta SOC d\tau. \quad (20)$$

K_{pSOC} and K_{iSOC} are the proportional and integral gain of the PI controller, and

$$\Delta K = K_0 \frac{\Delta Pwr}{Pwr_{avail}}. \quad (21)$$

Note that the SOC is in the range of [0, 90%] due to the compressible limit of the gas. Once the SOC is over 85%, the accumulator starts to store in less energy than requested. When SOC reaches its upper limit 90%, the accumulator completely stop working until it is requested to release energy. Similarly, when SOC is dropped down below 5%, the accumulator will start to release less energy than requested. When SOC gets to zero, the accumulator completely stop working until it is requested to store energy. We need guarantee the relatively smooth transition when we have to exclude the operation of accumulator. It will inevitably lead to a small period of variation in grid frequency due to the unbalance between power generation and load demand, but the frequency will be brought back to normal once the accumulator's SOC returns to [5%, 85%]. We have designed a proper controller to maintain the SOC within the range [5%, 85%].

By substituting the Pwr_0 and K_0 in (18) with ΔPwr

and ΔK , we will get the expression of $\Delta\tau_{pump}^*$. Then, the commanded torque τ_{pump}^* becomes

$$\tau_{pump}^*(\omega_r) = \tau_{pMAX}(\omega_r) + \Delta\tau_{pump}^*(\omega_r). \quad (22)$$

Note that the limit for $\Delta\tau_{pump}^*(\omega_r)$ is set to be $[-\tau_{pMAX}(\omega_r), 0.1\tau_{pMAX}(\omega_r)]$.

D. Pump-motor torque control

A PID pump-motor torque controller is designed to regulate the pump-motor torque τ_{pm} by adjusting the volumetric displacement of pump-motor D_{pm} . The system transfer function can be computed from (8), (9), (12) and (13) as

$$\tau_{pm}(s) = \frac{\eta\tau_{pm}p_0V_0D_{pm}^*}{(T_{pm}s + 1)(V_0 - \omega_g\eta Q_{pm}D_{pm}^* \cdot \frac{1}{T_{pm}s^2 + s} + \frac{1}{s}Q_{rv})}, \quad (23)$$

where D_{pm}^* , τ_{pm} and Q_{rv} are the system input, output and disturbance respectively. The control structure is shown in Fig. 3. A PID controller with a first order filter on derivative term is utilised:

$$D_{pm}^*(s) = (K_{pD_{pm}} + \frac{K_{iD_{pm}}}{s} + \frac{K_{dD_{pm}}s}{T_f s + 1})\Delta\tau_{pm}, \quad (24)$$

where $\Delta\tau_{pm} = \tau_{pm}^* - \tau_{pm}$. The parameters $K_{pD_{pm}}$, $K_{iD_{pm}}$, $K_{dD_{pm}}$ are the proportional, integral and derivative gain of the PID controller and T_f is the filter coefficient.

E. Relief valve protection control

In an emergency, such as abrupt lost of loads, the grid requests a sudden reduction in power generation in order to limit the frequency rise. Thence, a large amount of power has to be stored in the accumulator in a short time, since the response of pitch regulation is not fast enough to reduce the power extraction due to its mechanical response speed. In this case, the accumulator is at the risk of being overcharged, which can be protected by a relief valve. It starts operation when the hydraulic volume V_{hyd} in the accumulator reaches 80% of the accumulator total volume V_0 . When V_{hyd} reaches 85% of V_0 , the relief valve opens to its maximum.

The relief valve orifice area $A = \pi R_{ori}^2$ is controlled according to a tabulated function:

$$R_{ori} = \begin{cases} R_{min}, & SOC \leq 0.8; \\ R_{max}, & SOC \geq 0.85; \\ R_{min} + \frac{SOC - 0.8}{0.85 - 0.8}(R_{max} - R_{min}), & \text{otherwise}; \end{cases}$$

The unit for R_{ori} , R_{min} and R_{max} is meter (m).

F. Excitation control

On advantage of the utilization of synchronous generator, the reactive power can be controlled through an exciter unit. In this paper, a simplified DC exciter model [36] is applied, with the reference of terminal voltage selected to be

$$V_{ref} = 0.05 \cdot \int_0^\tau (Q_{ref} - Q) d\tau. \quad (25)$$

Note that the V_{ref} , Q_{ref} and Q are all expressed in p.u.

G. Frequency (active power) control

According to (10), τ_{pm} is a key term to stabilise the generator speed (or system frequency) under uncontrollable wind fluctuations and load variations. Hence, we need to compute a reference pump-motor torque τ_{pm}^* to compensate the difference between motor torque and electrical torque, which represents the difference between extracted power and grid request. Then, by proper pump-motor torque control, the real torque will be regulated to track this reference, thus stabilising the system frequency. A PI controller is applied to calculate the required power for the grid:

$$P_{cmd} = D_{cmd}P_{avail} + (K_{pfc} + \frac{K_{I_{fc}}}{s} + K_{D_{fc}}s)\Delta f, \quad (26)$$

where D_{cmd} is the power de-rating coefficient from the system operator. It can be adjusted due to the wind forecast or load forecast every few hours. We take it as a constant for simplicity in our simulations. Δf is the normalised frequency difference between 1 p.u. (60 Hz) and actual system frequency. K_{pfc} , $K_{I_{fc}}$ and $K_{D_{fc}}$ are the proportional, integral and derivative gain of the controller. Then, the pump-motor torque reference is expressed as:

$$\tau_{pm}^* = \tau_{motor} - \frac{P_{cmd}}{\omega_g}. \quad (27)$$

It serves as the reference for the PID pump-motor torque controller.

IV. SIMULATION STUDIES

The simulations are conducted in Matlab/Simulink. A 5-bus 3-generator grid model (see Fig. 6) is applied. Generator-1 is connected to the HWT and generator-2 is the swing bus. All the disturbance and frequency events are run under a high wind power penetration rate (roughly 24%) in this small network. See Table. I for the parameters of the system and controllers. Two different cases are discussed to show the performances of the proposed control scheme.

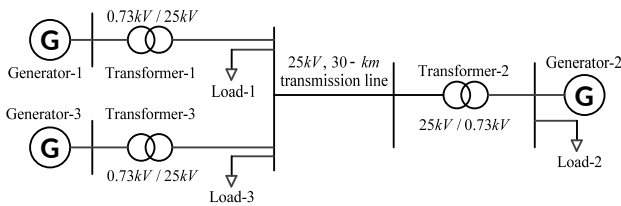
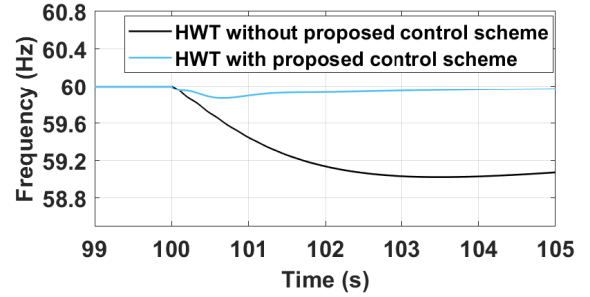


Fig. 6. Single line diagram of the grid model.

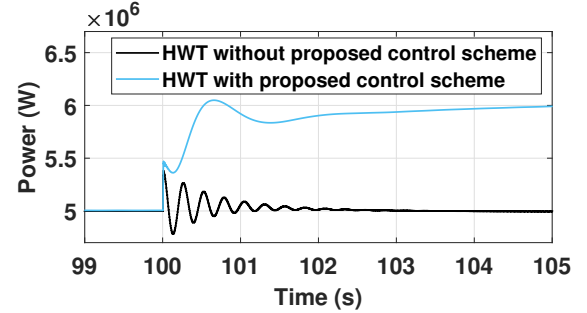
Case 1: Sudden lost of generation in the network

In this case, the small network of 21 MW is considered with a sudden loss of 1 MW (trip generator-3 at 100 second). The HWT operates under constant wind speed of 15 m/s. See Fig. 7 for the grid frequency response and HWT power output at the moment of generation lost. When the proposed control scheme is applied, the hydraulic accumulator releases the stored energy to the grid in a short time to stabilise the system frequency. However, after that, the other generator may

take over the responsibility of power delivery gradually. When the HWT operates without proposed control scheme, the power delivered from the HWT keeps at 5 MW. The swing bus will respond to the generation lost and gradually stabilise the system frequency. It is clear that better frequency response is achieved by the proposed control scheme due to the higher nadir and faster response.



(a) Grid frequency response.



(b) HWT power output.

Fig. 7. Comparison of the system dynamic response during sudden loss of Generator-3 with and without proposed control scheme of the HWT.

Case 2: Sudden load change and turbulent wind

A 500-second simulation is conducted to test the performances of the control scheme with variable load demand, under turbulent wind. Load-1 demand is changed every 100 seconds within the range of [2.5, 4.5] MW. NREL Turbsim [37] is utilised to generate stochastic, full-field, and turbulent wind flows for simulation studies. The International Electrotechnical Commission (IEC) Kaimal spectral NTM (normal turbulence model) in Turbsim is applied to generate the wind condition, with most turbulent characteristics (category A). The mean hub-height longitudinal wind speed is 11.4 m/s and the height for the reference wind speed is 90 m. The turbulence intensity in percentage is roughly 19.5%, and the standard deviation of the longitudinal wind speed at hub-height is approximately 2.22 m/s [37]. The wind speed series is generated with time step of 0.05 second. The wave is generated by using the JONSWAP irregular wave spectrum [38]. The significant wave height is set to be 6 meters, and the peak-spectral period of incident waves is set to be 10 seconds. Fig. 8 shows the turbulent wind, the rotor effective wind speed which is computed by FAST AeroDyn, and its estimations by LIDAR respectively, which implies LIDAR-estimated wind

TABLE I
SYSTEM AND CONTROL PARAMETERS

Symbol	Value	Unit	Symbol	Value	Unit	Symbol	Value	Unit
System Parameters								
C_{sp}	7.1×10^{-11}	$\text{m}^3/(\text{s}\cdot\text{Pa})$	C_{fp}	0.02	-	f_s	60	Hz
C_{sm}	7.0×10^{-11}	$\text{m}^3/(\text{s}\cdot\text{Pa})$	C_{fm}	0.02	-	ω_r^*	12.1	rpm
D_m	4.1609×10^{-4}	m^3/rad	B_p	50000	Nms	V_0	5	m^3
J_r	38759236	kgm^2	B_m	2.5	Nms	p_0	5	Mpa
J_p	3680	kgm^2	T_p	0.1	sec	$P_{\text{Generator}-1}$	6	MW
J_m	534.116	Kgm^2	T_{pm}	0.1	sec	$P_{\text{Generator}-2}$	15	MW
J_{pm}	50	kgm^2	η_{Qpm}	0.95	-	$P_{\text{Generator}-3}$	1	MW
J_g	50	kgm^2	η_{rpm}	0.98	-	$S_{\text{Load}-2}$	10	MVA
ρ_{sw}	1035	kg/m^3	C_D	0.7	-	$S_{\text{Load}-3}$	1	MVA
ν	1.05×10^{-6}	m^2/s	Re_{cr}	20	-	P_{wr0}	5.2966	MW
Control Parameters								
D_{cmd}	0.6	-	K_{pSOC}	1×10^8	-	T_f	0.0227	-
K_0	2128618.65	$\text{Nm}/(\text{rad}/\text{s})^2$	K_{ISOC}	4.42×10^5	-	SOC^*	0.7	-
Q_{ref}	0	MVar	$K_{pD_{pm}}$	5.63×10^{-7}	-	K_{pfc}	8.32×10^8	-
R_{min}	2×10^{-8}	m	$K_{ID_{pm}}$	8.65×10^{-6}	-	K_{Ifc}	2.12×10^8	-
R_{max}	0.2	m	$K_{DD_{pm}}$	3.84×10^{-9}	-	K_{Dfc}	2.11×10^7	-

speed tracks the low frequency trajectory of the rotor effective wind speed very well. Fig. 9-15 show the simulation results of the proposed coordinated control strategy.

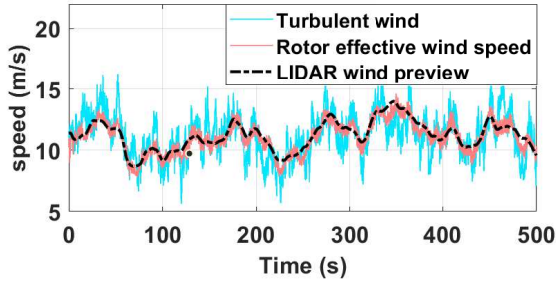


Fig. 8. Turbulent wind, rotor effective wind and LIDAR wind preview.

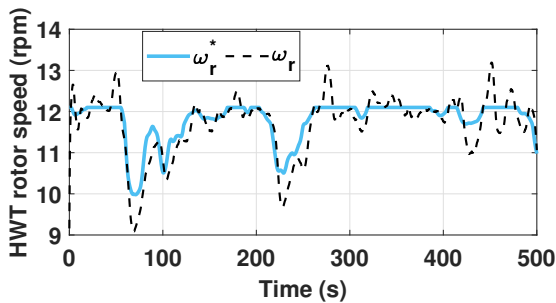


Fig. 9. Wind turbine rotor speed.

Fig. 9 shows the wind turbine rotor speed in revolution per minute (rpm) together with its reference ω_r^* , which is computed from the previewed wind speed (see Fig. 8) by LIDAR due to (14). The results indicate that actual wind turbine rotor speed ω_r roughly follows its reference ω_r^* by

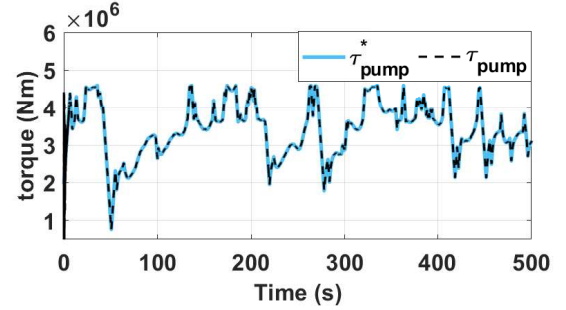


Fig. 10. Pump torque and its reference.

proper pitch control. The tracking performances of the \mathcal{H}_∞ loopshaping pump torque controller and PID pump-motor torque controller are both excellent, which are shown in Fig. 10 and Fig. 11 respectively. Fig. 12 shows the state-of-charge of the accumulator. It is controlled to stay at a relatively high level (70%) without exceeding its limit (90%). The fluctuation is mainly due to the wind conditions. Fig. 13 shows the output reactive power, which keeps at zero due to the effective excitation control. Fig. 14 shows the generator-1 power output, load-1 demand, wind turbine power extraction, and power flow in the accumulator. With proper coordination between the power extraction and power storage, the power output matches the load demand very well, indicating the effective regulation performance of the frequency (active power) controller in case of load variation with turbulent wind, see system frequency response in Fig. 15.

V. CONCLUSIONS

In this paper, we investigated the feasibility of the grid-integration of a converter-free offshore hydrostatic wind turbine (HWT) with frequency support capability. The ‘continuously variable gearbox ratio’ was realised by the proposed

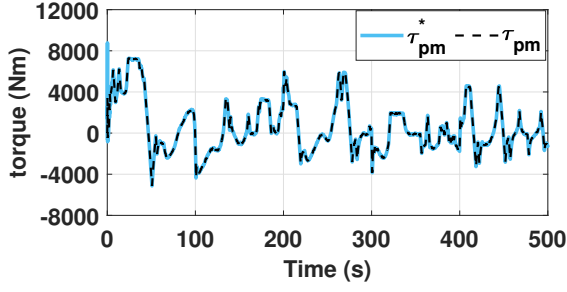


Fig. 11. Pump-motor torque and its reference.

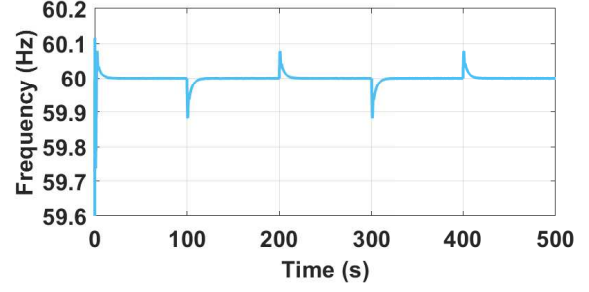


Fig. 15. System frequency response in Hz.

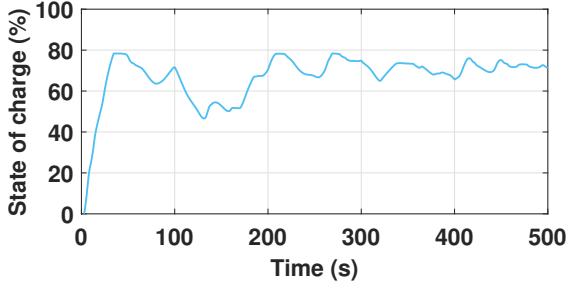


Fig. 12. State-of-charge (SOC) of the accumulator.

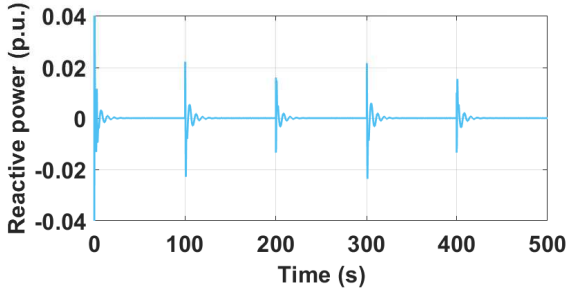


Fig. 13. Reactive power output of the generator-1.

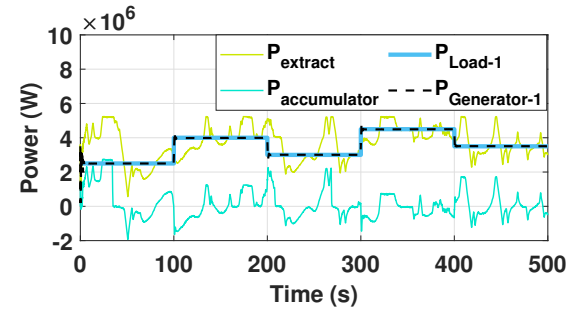


Fig. 14. Power extraction of wind turbine, power output of generator-1, load-1 demand and power flow of the accumulator.

hydrostatic transmission configuration from wind turbine rotor shaft to generator rotor shaft with the coordinated control strategy to maintain constant generator speed. This HWT was directly connected to the grid without power converters, just like a gas plant. In this way, it could provide direct inertia support to the system and participate in the grid frequency

response. The simulations indicated that the proposed coordinated control scheme had excellent performances under turbulent wind and variable loads, showing that it is a promising solution for offshore HWT in the frequency response with contribution to the electricity grid inertia.

The future work is to build a prototype HWT to validate the proposed system.

REFERENCES

- [1] Global Wind Energy Council, "Global Wind Report 2018," <https://gwec.net/wp-content/uploads/2019/04/GWEC-Global-Wind-Report-2018.pdf>, accessed: 25-06-2019.
- [2] World Wind Energy Association, "Wind Power Capacity Reaches 597GW, 50.1GW Added in 2018," <https://wwindea.org/blog/2019/02/25/wind-power-capacity-worldwide-reaches-600-gw-539-gw-added-in-2018/>, accessed: 25-06-2019.
- [3] Wind Europe, "Wind energy in Europe in 2018, Trends and Statistics," <https://windeurope.org/wp-content/uploads/files/about-wind/statistics/WindEurope-Annual-Statistics-2018.pdf>, accessed: 25-06-2019.
- [4] Y. Wang, J. Meng, X. Zhang, and L. Xu, "Control of pmsg-based wind turbines for system inertial response and power oscillation damping," *IEEE Transactions on Sustainable Energy*, vol. 6, no. 2, pp. 565–574, 2015.
- [5] Y. Wang, G. Delille, H. Bayem, X. Guillaud, and B. Francois, "High wind power penetration in isolated power systems: assessment of wind inertial and primary frequency responses," *IEEE Transactions on Power Systems*, vol. 28, no. 3, pp. 2412–2420, 2013.
- [6] J. Morren, S. W. De Haan, W. L. Kling, and J. Ferreira, "Wind turbines emulating inertia and supporting primary frequency control," *IEEE Transactions on power systems*, vol. 21, no. 1, pp. 433–434, 2006.
- [7] A. Buckspan, J. Aho, P. Fleming, Y. Jeong, and L. Pao, "Combining droop curve concepts with control systems for wind turbine active power control," in *Power Electronics and Machines in Wind Applications (PEMWA)*. Denver, CO, USA: IEEE, 2012, pp. 1–8.
- [8] L.-R. Chang-Chien, C.-C. Sun, and Y.-J. Yeh, "Modeling of wind farm participation in AGC," *IEEE Transactions on Power Systems*, vol. 29, no. 3, pp. 1204–1211, 2014.
- [9] W. Gao, Z. Wu, J. Wang, and S. Gu, "A review of inertia and frequency control technologies for variable speed wind turbines," in *25th Chinese Control and Decision Conference (CCDC)*. Guiyang, China: IEEE, 2013, pp. 2527–2533.
- [10] M. Dreidy, H. Mokhlis, and S. Mekhilef, "Inertia response and frequency control techniques for renewable energy sources: A review," *Renewable and Sustainable Energy Reviews*, vol. 69, pp. 144–155, 2017.
- [11] J. Aho, L. Pao, and P. Fleming, "An active power control system for wind turbines capable of primary and secondary frequency control for supporting grid reliability," in *51st AIAA Aerospace Sciences Meeting including the New Horizons Forum and Aerospace Exposition*, 2013, p. 456.
- [12] S. Wang, J. Hu, S. Wang, H. Tang, and Y. Chi, "Comparative study on primary frequency control schemes for variable-speed wind turbines," *The Journal of Engineering*, vol. 2017, no. 13, pp. 1332–1337, 2017.
- [13] F. Wilches-Bernal, J. H. Chow, and J. J. Sanchez-Gasca, "A fundamental study of applying wind turbines for power system frequency control," *IEEE Transactions on Power Systems*, vol. 31, no. 2, pp. 1496–1505, 2016.

- [14] J. Liang, S. Grijalva, and R. G. Harley, "Increased wind revenue and system security by trading wind power in energy and regulation reserve markets," *IEEE Transactions on Sustainable Energy*, vol. 2, no. 3, pp. 340–347, 2011.
- [15] S. Rybak, "Description of the 3 MW SWT-3 wind turbine at San Geronio Pass, California," 1982.
- [16] W. Rampen *et al.*, "Gearless transmissions of large wind turbines-the history and future of hydraulic drives," *Artemis IP Ltd., Midlothian, UK*, 2006.
- [17] J. Taylor, W. Rampen, A. Robertson, and C. Niall, "Digital displacement[®] hydraulic hybrids - parallel hybrid drives for commercial vehicles," vol. 1, 2011.
- [18] P. Silva, A. Giuffrida, N. Fergnani, E. Macchi, M. Cantú, R. Suffredini, M. Schiavetti, and G. Gigliucci, "Performance prediction of a multi-MW wind turbine adopting an advanced hydrostatic transmission," *Energy*, vol. 64, pp. 450–461, 2014.
- [19] M. Umay, T. Noguchi, M. Uchida, M. Shibata, Y. Kawai, and R. Notomi, "Wind power generation - development status of offshore wind turbines," *Mitsubishi Heavy Industries Technical Review*, vol. 50, no. 3, pp. 29 – 35, 2013.
- [20] J.-C. Ossyra, "Reliable, lightweight transmissions for off-shore, utility scale wind turbines," Eaton Corporation, Tech. Rep., 2012.
- [21] J. Carroll, A. McDonald, and D. McMillan, "Failure rate, repair time and unscheduled O&M cost analysis of offshore wind turbines," *Wind Energy*, vol. 19, no. 6, pp. 1107 – 1119, 2016.
- [22] X. Tong and X. Zhao, "Power generation control of a monopile hydrostatic wind turbine using an H_∞ loop-shaping torque controller and an LPV pitch controller," *IEEE Transactions on Control Systems Technology*, published online in 2017.
- [23] R. Dutta, F. Wang, B. F. Bohlmann, and K. A. Stelson, "Analysis of short-term energy storage for midsize hydrostatic wind turbine," *Journal of Dynamic Systems, Measurement, and Control*, vol. 136, no. 1, p. 011007, 2014.
- [24] F. Wang, J. Chen, B. Xu, and K. A. Stelson, "Improving the reliability and energy production of large wind turbine with a digital hydrostatic drivetrain," *Applied Energy*, vol. 251, p. 113309, 2019.
- [25] Y. Fan, A. Mu, and T. Ma, "Study on the application of energy storage system in offshore wind turbine with hydraulic transmission," *Energy Conversion and Management*, vol. 110, pp. 338–346, 2016.
- [26] M. Farbood, E. Taherian-Fard, M. Shasadeghi, A. Izadian, and T. Niknam, "Dynamics and control of a shared wind turbine drivetrain," *IEEE Transactions on Industry Applications*, vol. 54, no. 6, pp. 6394–6400, 2018.
- [27] J. M. Jonkman, M. L. Buhl Jr *et al.*, "FAST users guide," *National Renewable Energy Laboratory, Golden, CO, Technical Report No. NREL/EL-500-38230*, 2005.
- [28] M. Singh, E. Muljadi, J. Jonkman, V. Gevorgian, I. Girsang, and J. Dhupia, "Simulation for wind turbine generators with FAST and MATLAB-simulink modules," National Renewable Energy Laboratory (NREL), Golden, CO., Tech. Rep., 2014.
- [29] J. Jonkman, S. Butterfield, W. Musial, and G. Scott, "Definition of a 5-MW reference wind turbine for offshore system development," *National Renewable Energy Laboratory, Golden, CO, Technical Report No. NREL/TP-500-38060*, 2009.
- [30] A. J. Laguna, "Modeling and analysis of an offshore wind turbine with fluid power transmission for centralized electricity generation," *Journal of Computational and Nonlinear dynamics*, vol. 10, no. 4, p. 041002, 2015.
- [31] J. Makinen, P. Pertola, and H. Marjamaki, "Modeling coupled hydraulic-driven multibody systems using finite element method," in *1st Joint International Conference on Multibody System Dynamics, Lappeenranta University of Technology*, 2010.
- [32] M. Harris, M. Hand, and A. Wright, "LIDAR for turbine control," National Renewable Energy Laboratory (NREL), Golden, CO. No. NREL/TP-500-39154, Tech. Rep., 2006.
- [33] D.-W. Gu, P. Petkov, and M. M. Konstantinov, *Robust control design with MATLAB®*. Springer Science & Business Media, 2005.
- [34] Mathworks, "Control system toolbox reference (r2019a)," https://www.mathworks.com/help/pdf_doc/control/reference.pdf, retrieved on 25/06/2019.
- [35] G. Balas, R. Chiang, A. Packard, and M. Safonov, "Robust control toolbox reference (r2019a)," https://www.mathworks.com/help/pdf_doc/robust/robust_ref.pdf, retrieved on 25/06/2019.
- [36] I. W. Group *et al.*, "Recommended practice for excitation system models for power system stability studies," *IEEE Std 421.5-1992*, 1992.
- [37] B. J. Jonkman, "TurbSim user's guide: Version 1.50," National Renewable Energy Laboratory, CO, USA, Tech. Rep., 2009.
- [38] J. M. Jonkman and M. L. Buhl Jr, "Loads analysis of a floating offshore wind turbine using fully coupled simulation," National Renewable Energy Lab.(NREL), Golden, CO (United States), Tech. Rep., 2007.



search interests include renewable energy.

Shuyue Lin obtained her PhD in Engineering in 2019 from the University of Warwick, UK. Before that, she was an electrical engineer at Fujian Electric Power Survey and Design Institute in China. In 2013, she obtained her MSc (Distinction) in Control systems from Imperial College London, UK. In 2012, she obtained her BEng degrees (First Class Honours) in Electrical Power Engineering from University of Bath (UK) and BEng degree in Electrical Power Engineering & Automation from North China Electric Power University (China). Her current research interests include the power generation and grid integration of the



bridges; (3) Control of coupled infinite-dimensional systems; (4) Microgrid.

Xiaowei Zhao is Professor of Control Engineering at the University of Warwick in the UK. He obtained his PhD degree in Control Theory from Imperial College London in the UK in 2010. After that he worked as a postdoctoral researcher at the University of Oxford in the UK for three years before joining Warwick in 2013. His research interests include (1) Control of wind turbines/wind farms and their grid integration; (2) Control of fluid-structure interaction with applications to large & flexible wind turbines, highly flexible aircraft, and long-span suspension



Xin Tong is a research engineer in Jaguar Land Rover Limited. She obtained her PhD in Engineering in 2017 from the University of Warwick, UK. She obtained her MSc (Distinction) in Control Systems in 2013 from Imperial College London in the UK, and obtained her BEng in Electrical Engineering & Automation in 2012 from Huazhong University of Science and Technology in China. Her current research interest is control of large offshore wind turbines, and powertrain control & calibration.